Journal of Computational Physics **150,** 373–393 (1999)
Article ID jcph.1999.6198, available online at http://www.idealibrary.com on IDEAL®

A Roe Scheme for Ideal MHD Equations on 2D Adaptively Refined Triangular Grids

P. F. Peyrard*,† and P. Villedieu‡

*ONERA, Centre d'Etudes et de Recherches de Toulouse, DESP, 2 Avenue Edouard Belin, 31055 Toulouse Cedex, France; †Mathématiques pour l'Industrie et la Physique, UMR CNRS 5640, URF MIG, Université Paul Sabatier, 118, Route de Narbonne, 31062 Toulouse Cedex, France; ‡ONERA, Centre d'Etudes et de Recherches de Toulouse, DTIM/M2SN, 2 Avenue Edouard Belin, 31055 Toulouse Cedex, France
E-mail: pierre-francois.peyrard@onecert.fr, philippe.villedieu@onecert.fr

Received December 2, 1997; revised December 24, 1998

In this paper we present a second order finite volume method for the resolution of the bidimensional ideal MHD equations on adaptively refined triangular meshes. Our numerical flux function is based on a multidimensional extension of the Roe scheme proposed by Cargo and Gallice for the 1D MHD system. If the mesh is only composed of triangles, our scheme is proved to be weakly consistent with the condition $\nabla \cdot \mathbf{B} = 0$. This property fails on a cartesian grid. The efficiency of our refinement procedure is shown on 2D MHD shock capturing simulations. Numerical results are compared in case of the interaction of a supersonic plasma with a cylinder on the adapted grid and several non-refined grids. We also present a mass loading simulation which corresponds to a 2D version of the interaction between the solar wind and a comet.

Key Words: magnetohydrodynamics; finite volume method; Roe scheme; non-parametrized entropy correction; 2D simulations; unstructured grid; adaptive refinement.

1. INTRODUCTION

Astrophysicists are more and more interested in the numerical simulation of the ideal MHD equations in order to study space plasma flows. In recent years, approximate Riemann solvers have been developed for this hyperbolic system, but most of the papers concern 1D applications.

Brio and Wu [4] have constructed the eigensystem of a Roe matrix in the special case $\gamma = 2$. Dai and Woodward [8, 9] have proposed an approximate Riemann solver which is only based on discontinuity waves. The method developed by Bell, Colella, and Trangenstein [2] for hydrodynamic applications has been extended to the MHD equations by Zachary and Colella in [21]. Croisille, Khanfir, and Chanteur have introduced a kinetic formalism

0021-9991/99 $30.00

for the MHD system and derived a kinetic type solver [7]. All these methods have been first tested on the Brio and Wu shock tube, but the numerical simulation of multidimensional flows presents additional difficulties, especially the conservation of the condition $\nabla \cdot \mathbf{B} = 0$.

To deal with this constraint, different approaches have been investigated. Schmidt-Voigt [16] and Tanaka [17] proposed adding a correction of $\mathbf{B}$ at each time step, but they needed to solve an elliptic equation, which significantly increases the CPU time of a calculation. To avoid this problem, Aslan and Kammash [1] and Powell [14] proposed modifying the MHD equations by introducing an additional source term, proportional to $\nabla \cdot \mathbf{B}$. The result of this modification is that $\nabla \cdot \mathbf{B}$ is then the solution of a transport equation which convects it out of the domain.

In this paper, we present a simpler approach. We adapt the 1D Roe scheme of Cargo and Gallice [6, 5, 11] to derive a multidimensional numerical flux function and, as in [7], no particular treatment is done to enforce the condition $\nabla \cdot \mathbf{B} = 0$. Since we use triangular grids and the numerical flux related to the magnetic field is parallel to the interface of the cells, this constraint is verified in a weak sense, as for the kinetic scheme of Croisille *et al.* [7]. We emphasize the necessity of using triangular grids. This property is not satisfied any more on a cartesian grid, as it will be proved numerically in Section 4.

The paper is organised as follows. Section 2 is devoted to the description of our numerical method and the refinement procedure. In Section 3, the weak consistency of the scheme with the constraint $\nabla \cdot \mathbf{B} = 0$ is analysed from a theoretical and numerical point of view. The last part of the paper is devoted to 2D hypersonic plasma flows calculations. It is shown, in this context, the efficiency of adaptively refined triangular grids.

2. DESCRIPTION OF THE NUMERICAL METHOD

2.1. *Ideal MHD Model*

We consider a one fluid ideal MHD model where the plasma is described by averaged macroscopic quantities. Under the following assumptions, quasineutrality, isotropy of the pressure tensor, infinite conductivity, and adiabaticity, the following set of equations can be derived [19] (scaling conventions in [12]),

$$\frac{\partial}{\partial t}\begin{pmatrix} \rho \\ \rho\mathbf{u} \\ \mathbf{B} \\ E \end{pmatrix} + \nabla \cdot \begin{pmatrix} \rho\mathbf{u} \\ \rho\mathbf{u}\otimes\mathbf{u} + I\left(p + \frac{\mathbf{B}\cdot\mathbf{B}}{2}\right) - \mathbf{B}\otimes\mathbf{B} \\ \mathbf{B}\otimes\mathbf{u} - \mathbf{u}\otimes\mathbf{B} \\ \left(E + p + \frac{\mathbf{B}\cdot\mathbf{B}}{2}\right)\mathbf{u} - (\mathbf{u}\cdot\mathbf{B})\mathbf{B} \end{pmatrix} = 0 \tag{1}$$

with the constraint

$$\nabla \cdot \mathbf{B} = 0. \tag{2}$$

Here ρ, $\mathbf{u}$, $\mathbf{B}$, and p are the density, the velocity, the magnetic field, and the pressure. The energy E is given by the state equation

$$E = \frac{p}{\gamma - 1} + \rho\frac{\mathbf{u}\cdot\mathbf{u}}{2} + \frac{\mathbf{B}\cdot\mathbf{B}}{2}, \tag{3}$$

where γ is the ratio of specific heats. The electric field $\mathcal{E}$ satisfies the frozen-in-field equation

$$\mathcal{E} = -\mathbf{u} \wedge \mathbf{B}. \tag{4}$$

To define a finite volume scheme, it is sufficient to solve 1D Riemann problems at each interface of the grid. The 1D projection (according to the coordinate n) of the system (1), (2) modifies its structure. The 1D constraint applied to (2) gives $\partial B_n/\partial n = 0$; the 1D constraint applied to the Faraday equation results in $\partial B_n/\partial t = 0$ and hence

$$B_n = \textit{constant} \tag{5}$$

and the 1D system consists of the seven equations parametrized by B_n,

$$\frac{\partial W}{\partial t} + \frac{\partial F_{B_n}(W)}{\partial n} = 0 \tag{6}$$

with

$$W = \begin{pmatrix} \rho \\ \rho u_n \\ \rho u_\xi \\ \rho u_z \\ B_\xi \\ B_z \\ E \end{pmatrix}, \qquad F_{B_n}(W) = \begin{pmatrix} \rho u_n \\ \rho u_n^2 + p + \frac{\mathbf{B}\cdot\mathbf{B}}{2} \\ \rho u_n u_\xi - B_n B_\xi \\ \rho u_n u_z - B_n B_z \\ u_n B_\xi - u_\xi B_n \\ u_n B_z - u_z B_n \\ \left(E + p + \frac{\mathbf{B}\cdot\mathbf{B}}{2}\right) u_n - \left(u_n B_n^2 + u_\xi B_n B_\xi + u_z B_n B_z\right) \end{pmatrix}, \tag{7}$$

ξ and z are the cartesian coordinates in the plane perpendicular to the axis n.

2.2. *Numerical Scheme*

Let us denote by K any cell of the mesh, K_e the neighbour of K along the edge e, $\mathbf{n_{e,K}}$ the unit normal vector on e oriented from K to K_e, and Δt the time step (see Fig. 1).

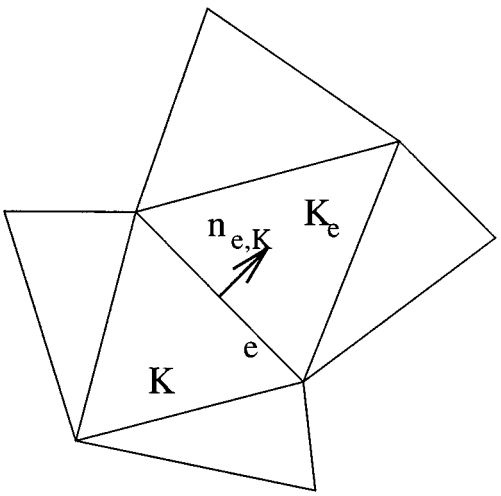

FIG. 1. Part of a 2D triangulation.

The general expression of a finite volume scheme for the system (1) is

$$U_K^{n+1} = U_K^n - \frac{\Delta t}{|K|} \sum_{e \in \partial K} \Phi\big(U_K^n, U_{Ke}^n, \mathbf{n}_{\mathbf{e},K}\big)|e|, \tag{8}$$

where U_K^n is the value of the approximate solution $U_h(t, \mathbf{x})$ on the cell K between times t^n and t^{n+1}, $|K|$ is the surface of K, and $\Phi(U, V, \mathbf{n})$ the numerical flux in the direction of the vector $\mathbf{n}$. In our case, it has the expression

$$\Phi(U, V, \mathbf{n}) = T_{\mathbf{n}}^{-1} \begin{pmatrix} \Phi_{\mathbf{n}}^{\mathrm{Roe}}(P_{\mathbf{n}}(U), P_{\mathbf{n}}(V)) \\ 0 \end{pmatrix}, \tag{9}$$

where the $T_{\mathbf{n}}$, respectively $P_{\mathbf{n}}$, are mappings from $\mathbb{R}^8$ onto $\mathbb{R}^8$, respectively $\mathbb{R}^8$ onto $\mathbb{R}^7$, defined as

$$T_{\mathbf{n}}(U) = T_{\mathbf{n}} \begin{pmatrix} \rho \\ \rho u_x \\ \rho u_y \\ \rho u_z \\ B_x \\ B_y \\ B_z \\ E \end{pmatrix} = \begin{pmatrix} \rho \\ \rho u_n \\ \rho u_\xi \\ \rho u_z \\ B_\xi \\ B_z \\ E \\ B_n \end{pmatrix} = \begin{pmatrix} P_{\mathbf{n}}(U) \\ B_n \end{pmatrix},$$

where (n, ξ, z) are the coordinates related to the edge and $\Phi_{\mathbf{n}}^{\mathrm{Roe}}$ is a Roe numerical flux related to the 1D system (6)–(7). We have chosen to adapt the 1D Roe scheme proposed by Cargo and Gallice in [6]. It leads to the following expression for $\Phi_{\mathbf{n}}^{\mathrm{Roe}}$,

$$\begin{aligned} \Phi_{\mathbf{n}}^{\mathrm{Roe}}(U, V) &= \frac{1}{2}\big(F_{B_n}(P_{\mathbf{n}}(U)) + F_{B_n}(P_{\mathbf{n}}(V))\big) \\ &\quad - \big|A_{B_n}^{\mathrm{Roe}}\big|(P_{\mathbf{n}}(U), P_{\mathbf{n}}(V))[P_{\mathbf{n}}(V) - P_{\mathbf{n}}(U)] \\ &= \frac{1}{2}\big(F_{B_n}(P_{\mathbf{n}}(U)) + F_{B_n}(P_{\mathbf{n}}(V))\big) - \sum_{k=1}^{7} \alpha_{\lambda_k} |\lambda_k| R_{\lambda_k}, \end{aligned} \tag{10}$$

where $A_{B_n}^{\mathrm{Roe}}$ is the Roe matrix of Cargo and Gallice related to the flux F_{B_n}. The characteristic variables α_{λ_k} are defined by

$$\alpha_{\lambda_k} = L_{\lambda_k} \cdot [P_{\mathbf{n}}(V) - P_{\mathbf{n}}(U)], \qquad k = 1, 7, \tag{11}$$

where L_{λ_k}, $k = 1, 7$, are the left eigenvectors of $A_{B_n}^{\mathrm{Roe}}$. Since the normal component of the magnetic field B_n is not necessarily the same on each side of an edge, a choice has to be made to define the value of B_n that will be used in the expression of the Roe matrix. In the Roe matrix, the same average procedure is applied for B_ξ and B_z (see [6]). Hence this average has also been chosen for B_n,

$$B_{n,e} = \frac{\sqrt{\rho_K} B_{n,Ke} + \sqrt{\rho_{Ke}} B_{n,K}}{\sqrt{\rho_K} + \sqrt{\rho_{Ke}}}.$$

2.3. *Second Order Extension*

The second order accuracy of the scheme in space and time is ensured by a MUSCL-type method and an explicit Runge–Kutta scheme for the time discretization.

Let U^n be the values of the state U at time t^n. We first calculate $U^{n+1/2}$ at time $t^n + \frac{\Delta t}{2}$ by using the first order scheme (8)–(10). Those "predicted values" are then used to evaluate an approximation of the gradient of the discrete solution. For any given primitive variable u associated with U, its gradient on the cell K is estimated by

$$(\nabla u)_K = \frac{1}{|K|} \sum_{e \in \partial K} u_e \mathbf{n}_{e,K} |e|$$

with u_e defined as a simple average

$$u_e = \frac{1}{2}(u_K + u_{Ke}).$$

Classically, in order to avoid the creation of new extrema in the linear reconstructed solution, the gradients have to be limited. For each cell $K \in \mathcal{T}_h$, $(\nabla u)_K$ is replaced by $\overline{(\nabla u)}_K$, with

$$\begin{aligned} \overline{(\nabla u)}_K &= \alpha_K (\nabla u)_K \\ \alpha_K &= \min(1, \alpha_{max}, \alpha_{min}) \\ \alpha_{max} &= \frac{u_{max} - u_m}{\Delta_{max}} \\ \alpha_{min} &= \frac{u_m - u_{min}}{\Delta_{min}}, \end{aligned}$$

where $u_{max} = \mathrm{Max}_{e \in \partial K}(u_{Ke})$, $u_{min} = \mathrm{Min}_{e \in \partial K}(u_{Ke})$, $u_m = \mathrm{Max}(u_{min}, \mathrm{Min}(u_K, u_{max}))$, $\Delta_{max} = \mathrm{Max}_{x \in K} |(\nabla u)_K \cdot (\mathbf{x} - \mathbf{x_K})|$, $\Delta_{min} = \mathrm{Min}_{x \in K} |(\nabla u)_K \cdot (\mathbf{x} - \mathbf{x_K})|$, x_K denotes the center of K. For near-uniform regions, we have $\Delta_{max} \simeq 0$ and $\Delta_{min} \simeq 0$, so we use a lower limit (e.g., 10^{-30}) for those values in order to avoid degeneracy of the calculation. This limiter is not very compressive (see, for example, the numerical study [18]) but seems to be robust enough to avoid instabilities near strong discontinuities.

Finally the values of U at time t^{n+1} are defined as

$$U_K^{n+1} = U_K^n - \frac{\Delta t}{|K|} \sum_{e \in \partial K} \Phi\left(U_{e,K}^{n+\frac{1}{2}}, U_{e,Ke}^{n+\frac{1}{2}}, \mathbf{n_{e,K}}\right) |e| \tag{12}$$

with $U_{e,K}^{n+1/2}$ the interpolated values of $U^{n+1/2}$ at the midpoint x_e of the edge e of K:

$$U_{e,K}^{n+\frac{1}{2}} = U_K^{n+\frac{1}{2}} + \overline{(\nabla U)}_K \cdot (\mathbf{x_e} - \mathbf{x_K}).$$

2.4. *Description of the Mesh Adaptation Technique*

The shock capturing problem in astrophysics is the main application of our code. This kind of problem generally involves multiscale phenomena. To have both great accuracy and

small CPU time, the solution is to use adaptive refinement, which is now widely applied in CFD methods (see, for example, [15, 12] and the references therein).

Our mesh adaptation strategy consists of a local enrichment of the initial grid by adding some new cells to the area where the refinement sensor is too high. Our sensor is based on the gradient of the sonic mach number; it has the expression

$$R_K = \left| \nabla \left(\frac{|V|}{c} \right)_K \right|, \tag{13}$$

where $|V|$ is the velocity modulus and c is sound speed given by

$$c = \sqrt{\frac{\gamma p}{\rho}}.$$

A more appropriate sensor should involve magnetic terms. However, for our applications, this "hydrodynamic sensor" is accurate enough to detect interesting cells which have to be refined.

When the steady steady state is reached on the initial coarse mesh, the refinement sensor R_K is calculated in each cell; then the elements are ordered from the highest value of R_K to its lowest. At this stage, the number of cells that have to be refined can be chosen in two different ways:

(i) by imposing their number,
(ii) by imposing the lowest value of the sensor above which a cell has to be refined.

The advantage of the first solution is to ensure a control of the number of cells in the adapted mesh. Then our refinement technique consists in dividing each selected triangle, independent of its neighbours, into 4 "child triangles" as illustrated in Fig. 2. Note that each new element is homothetic (up to a rotation) to its parent, it means that new edges are exactly parallel to edges of the parent cell. This avoids the creation of a degenerated triangle, but the adapted grid is a non-conformal triangulation (hanging nodes are created).

Finally the solution on the created mesh is initialized with the one calculated on the initial coarse grid and a new calculation is performed until convergence to the steady state. Of course, all of this process can be performed again if the solution on the refined mesh is not precise enough.

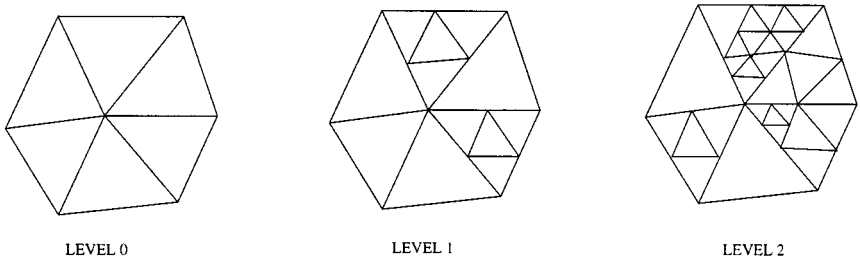

FIG. 2. The 2 iterations of the refinement procedure. The resulting mesh is a non-conformal triangulation.

2.5. *Entropy Correction*

A well known default of the Roe scheme is that it can generate a shock which violates the entropy condition. A possible solution to deal with this drawback is to use Harten's classical entropy fix; alternative approaches are also possible (see, for example, [1, 10]).

The main idea of Harten's entropy correction (see [13]) is to introduce some numerical viscosity in the vicinity of sonic points. Since a non-entropic discontinuity may only appear when an eigenvalue tends to 0, the numerical flux (10) is modified by changing the eigenvalues $|\lambda|$ by $\Psi(\lambda)$ with (see [13]),

$$\Psi(\lambda) = \begin{cases} |\lambda|, & |\lambda| \geq \delta \\ \frac{(\lambda^2+\delta^2)}{2\delta}, & |\lambda| < \delta, \end{cases} \tag{14}$$

where δ controls the amplitude of the additional artificial viscosity. In case of hypersonic flows, δ is chosen as

$$\delta = \tilde{\delta}(|u| + c_f) \tag{15}$$

with $u + c_f$ as the fast magnetosonic eigenvalue of the Roe matrix. It means that, in some cases, the parameter $\tilde{\delta}$ has to be tuned until some spurious instabilities are damped. In [20], the control of the size of $\tilde{\delta}$ has been investigated in the case of hypersonic flows around a blunt body.

3. CONSISTENCY WITH THE CONSTRAINT $\nabla \cdot \mathbf{B} = 0$

A weak consistency of the scheme (8)–(10) with the constraint $\nabla \cdot \mathbf{B} = 0$ can be proved under general hypothesis. In [3], F. Bouchut studies numerical methods which exactly preserve the Gauss–Poisson equation when solving the charge conservation and Maxwell–Ampère equations. His idea has been directly applied to the conservation of $\nabla \cdot \mathbf{B} = 0$ in the case of MHD equations in [7]. We recall here this result.

Let $\mathcal{T}_h$ be a conformal triangulation.

Let $\mathcal{N}_h$ be the set of all vertices in $\mathcal{T}_h$.

Let φ_N ($N \in \mathcal{N}_h$) be the piecewise affine function (P^1-Lagrange function) such that

$$\varphi_N(x) = \begin{cases} 1 & \text{for } \mathbf{x} = \mathbf{x}_N \\ 0 & \text{for } \mathbf{x} = \mathbf{x}_{N'}\ \forall N' \in \mathcal{N}_h \text{ and } N' \neq N. \end{cases} \tag{16}$$

Then if, for each edge, the numerical flux related to the Faraday equation is parallel to the edge, then

$$\forall n \in \mathbb{N}, \forall N \in \mathcal{N}_h, \qquad \int_{\mathbb{R}^2} \left(\mathbf{B}_\mathbf{h}^{\mathbf{n+1}} - \mathbf{B}_\mathbf{h}^{\mathbf{n}}\right) \cdot \nabla \varphi_N \, dx = 0, \tag{17}$$

where $\mathbf{B}_\mathbf{h}^{\mathbf{n}}$ is the piecewise constant function such that $\forall x \in K$, $\mathbf{B}_\mathbf{h}^{\mathbf{n}}(x) = \mathbf{B}_\mathbf{K}^{\mathbf{n}}$. If the initial condition $\mathbf{B}_\mathbf{h}^{\mathbf{0}}$ is such that

$$\forall N \in \mathcal{N}_h, \qquad \int_{\mathbb{R}^2} \mathbf{B}_\mathbf{h}^{\mathbf{0}} \cdot \nabla \varphi_N \, dx = 0, \tag{18}$$

then (17) yields

$$\forall N \in \mathcal{N}_h, \qquad \int_{\mathbb{R}^2} \mathbf{B}_\mathbf{h}^{\mathbf{n}} . \nabla \varphi_N \, dx = 0. \tag{19}$$

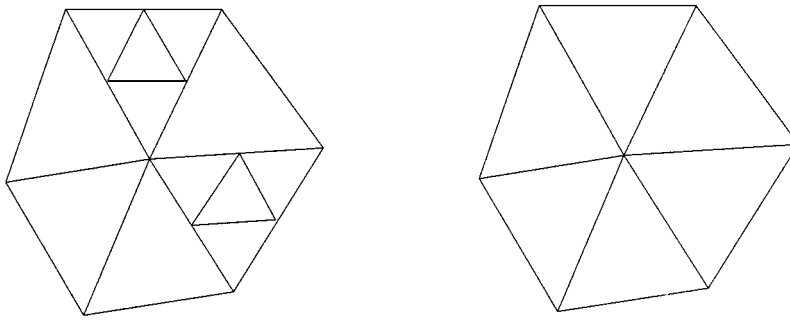

FIG. 3. Correspondence between cells of $\mathcal{T}_h$ and $\mathcal{T}_h^0$.

Equation (19) is a weak formulation of the equation $\nabla \cdot \mathbf{B} = 0$. That's the reason why this property is called "weak consistency."

In our case, by construction of the scheme, at each edge, the perpendicular component of the magnetic numerical flux is zero (because B_n *is constant*), but, because of the refinement procedure, there are some hanging nodes in the grid. So the previous result has to be extended to such triangular meshes.

Let $\mathcal{T}_h^0$ be the primary conformal triangular grid (see Fig. 3), $\mathcal{S}_h^0$ the set of all edges in $\mathcal{T}_h^0$, $\mathcal{N}_h^0$ the set of all vertices in $\mathcal{T}_h^0$, $\mathcal{T}_h$ the resulting mesh after an arbitrary number of refinement stages, and $\mathcal{S}_h$ the set of all edges in $\mathcal{T}_h$. The numerical scheme (8)–(10) is consistent with the condition $\nabla \cdot \mathbf{B} = 0$ in the following sense:

WEAK CONSISTENCY PROPERTY. *For any $N \in \mathcal{N}_h^0$, let φ_N be the P^1-Lagrange function defined as φ_N is piecewise linear on any cell of $\mathcal{T}_h^0$ and*

$$\varphi_N(x) = \begin{cases} 1 & \text{for } \mathbf{x} = \mathbf{x}_N \\ 0 & \text{for } \mathbf{x} = \mathbf{x}_{N'}\ \forall N' \in \mathcal{N}_h^0 \text{ and } N' \neq N. \end{cases} \tag{20}$$

The scheme (8)–(10) *verifies the property*

$$\forall n \in \mathbb{N}, \forall N \in \mathcal{N}_h^0, \qquad \int_{\mathbb{R}^2} \left(\mathbf{B_h^{n+1}} - \mathbf{B_h^n}\right) \cdot \nabla \varphi_N \, dx = 0. \tag{21}$$

Remarks.

- This means that if the initial solution satisfies $\nabla \cdot \mathbf{B} = 0$, this constraint will be preserved in a weak sense at each time step. However, note that theoretically, (21) does not prevent the accumulation of numerical approximation errors. But numerical results of the next section will show that those errors remain negligible.
- The result is still true in 3D for tetrahedral meshes.

Proof. Our proof is a direct extension of the proof given in [7]. Let (Ω_N) be the support of φ_N (Fig. 4).

The finite volume formulation (8) yields

$$\mathbf{B}_K^{n+1} = \mathbf{B}_K^n - \frac{\Delta t}{|K|} \sum_{e \in \partial K} \Phi_B\left(U_K^n, U_{Ke}^n, \mathbf{n_{e,K}}\right)|e|. \tag{22}$$

Equation (22) yields easily

$$\int_{\mathrm{R}^2} \left(\mathbf{B_h^{n+1}} - \mathbf{B_h^n}\right) \cdot \nabla \varphi_N \, d\mathbf{x} = -\Delta t \sum_{K \in \Omega_N,\, e \in \partial K} \nabla \varphi_{K,N} \cdot \Phi_B\left(U_K^n, U_{Ke}^n, \mathbf{n_{e,K}}\right) |e| \tag{23}$$

since in any $K \in \Omega_N \cap \mathcal{T}_h^0$, $\nabla \varphi_N$ is constant, $\nabla \varphi_{K,N}$ denoting its value in K. Conservation of the scheme gives

$$\Phi_B\left(U_K^n, U_{Ke}^n, \mathbf{n_{e,K}}\right) = -\Phi_B\left(U_{Ke}^n, U_K^n, \mathbf{n_{e,Ke}}\right). \tag{24}$$

So by (23), we get

$$\begin{aligned}\int_{\mathrm{R}^2} \left(\mathbf{B_h^{n+1}} - \mathbf{B_h^n}\right) \cdot \nabla \varphi_N \, d\mathbf{x} = &-\Delta t \sum_{e \in \Omega_N} (\nabla \varphi_{K,N} - \nabla \varphi_{Ke,N}) \cdot \Phi_B\left(U_K^n, U_{Ke}^n, \mathbf{n_{e,K}}\right) |e| \\ &- \Delta t \sum_{e \in \partial \Omega_N} \nabla \varphi_{K,N} \cdot \Phi_B\left(U_K^n, U_{Ke}^n, \mathbf{n_{e,K}}\right) |e|. \end{aligned} \tag{25}$$

So we can distinguish three types of edges:

(i) The edge e is of type 1 ($e \subset \partial \Omega_N$). Since $\Phi_B(U_K^n, U_{Ke}^n, \mathbf{n_{e,K}}) // e$ and $\varphi_{K,N} = -(|e_{K,N}|/2|K|) n_{K,N}$ (the notations $n_{K,N}$ and $e_{K,N}$ are defined in Fig. 4), we have $\nabla \varphi_{K,N} \cdot \Phi_B(U_K^n, U_{Ke}^n, \mathbf{n_{e,K}}) = 0$.

(ii) The edge e is of type 3 ($e \subset \mathcal{S}_h$ and $e \not\subset \mathcal{S}_h^0$). By definition of φ_N, we have $\nabla \varphi_{K,N} = \nabla \varphi_{Ke,N}$ so

$$(\nabla \varphi_{K,N} - \nabla \varphi_{Ke,N}) \cdot \Phi_B\left(U_K^n, U_{Ke}^n, \mathbf{n_{e,K}}\right) = 0.$$

(iii) The edge e is of type 2 ($e \subset \mathcal{N}_h^0$ and $e \not\subset \partial \Omega_N$). Since $\varphi_{K,N} = \varphi_{Ke,N}$ along e and $\Phi_B(U_K^n, U_{Ke}^n, \mathbf{n_{e,K}}) // e$, we have $(\nabla \varphi_{K,N} - \nabla \varphi_{Ke,N}) \cdot \Phi_B(U_K^n, U_{Ke}^n, \mathbf{n_{e,K}}) = 0$.

Finally, taking into account (i), (ii), (iii), we get

$$\sum_{K \in \Omega_N,\, e \in \partial K} \nabla \varphi_N \cdot \Phi_B\left(U_K^n, U_{Ke}^n, \mathbf{n_{e,K}}\right) |e| = 0$$

hence

$$\int_{\mathrm{R}^2} \left(\mathbf{B_h^{n+1}} - \mathbf{B_h^n}\right) \cdot \nabla \varphi_N \, d\mathbf{x} = 0$$

which is the desired result. ■

Note that, φ_N being the P^1-Lagrange function related to the node N of a triangular grid, the vector $\nabla \varphi_N$ is constant on each cell K surrounding N and its special orientation gives step (i) of the proof. This fundamental feature of the test functions is no more satisfied for Q^1 functions on a rectangular grid. So we cannot expect the constraint $\nabla \cdot \mathbf{B} = 0$ to be preserved on cartesian grids as will be numerically shown below.

To test the numerical validity of this weak consistency property on general triangular meshes, calculations have first been performed on the classical shock tube problem of Brio and Wu [4]. This problem is physically monodimensional (but the grid is 2D), so the normal component of B is expected to remain constant. All the following numerical calculations have been performed with the Roe scheme with the second order extension.

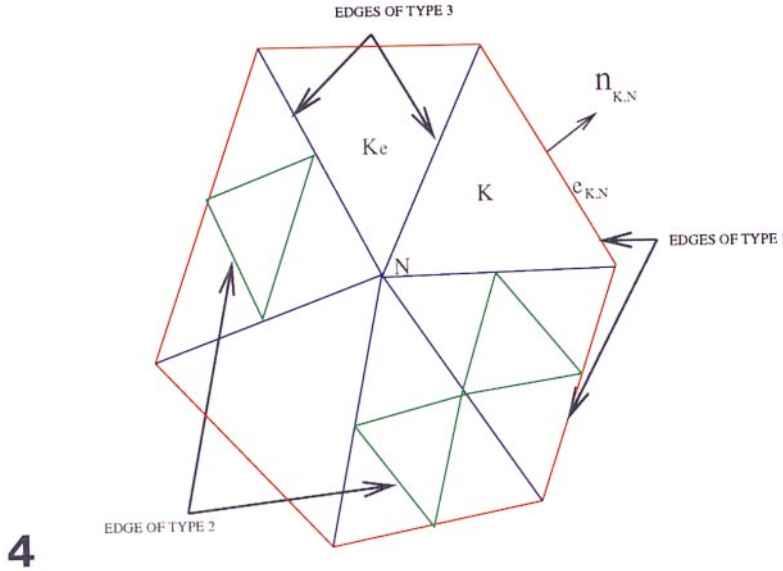

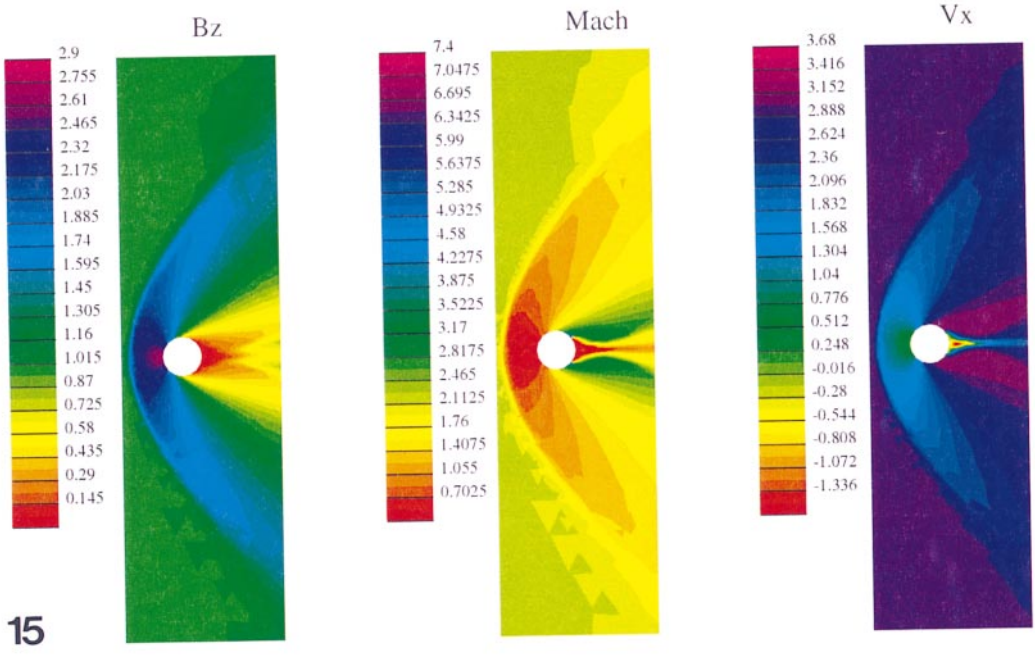

FIG. 4. Support of φ_N.

FIG. 15. Results on the refined grid.

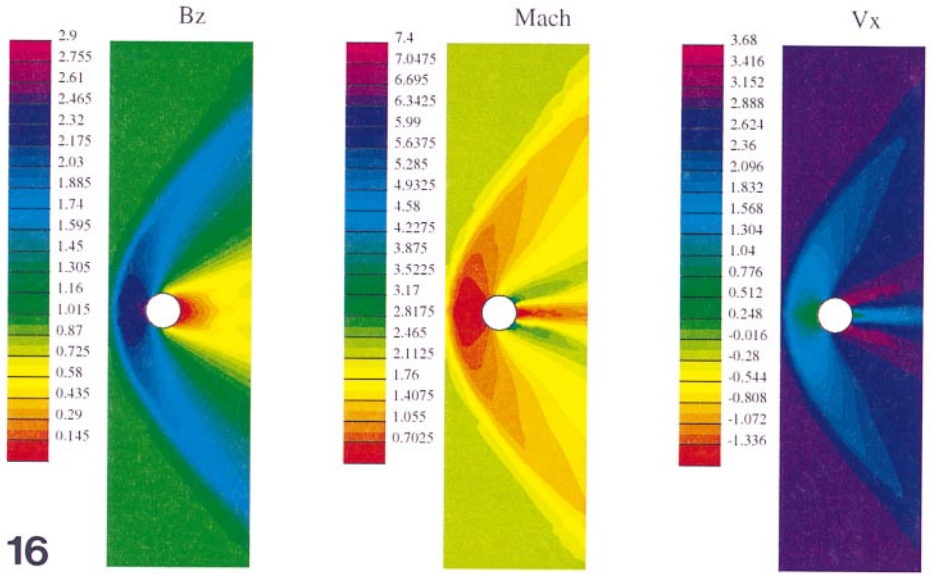

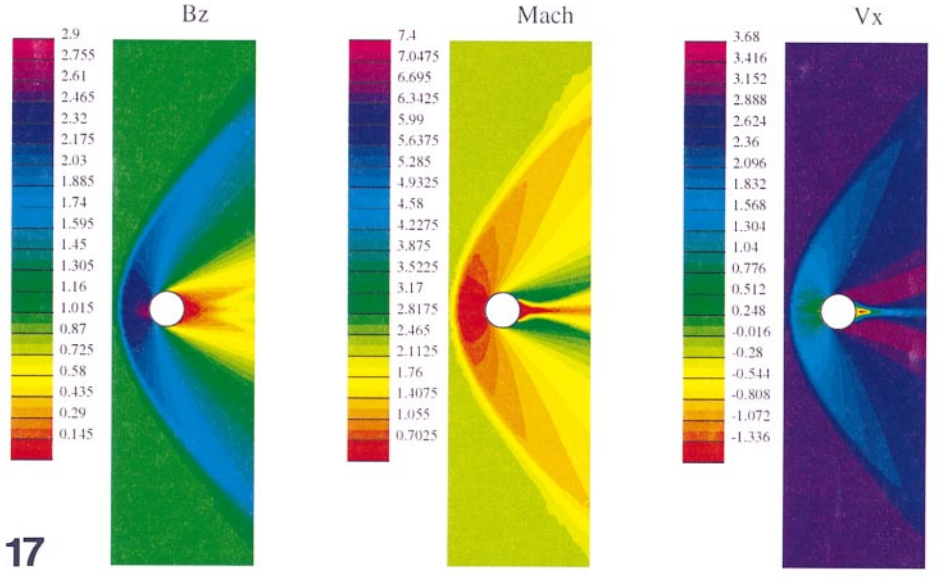

FIG. 16. Results on the 7000 elements grid.

FIG. 17. Results on the 20,000 elements grid.

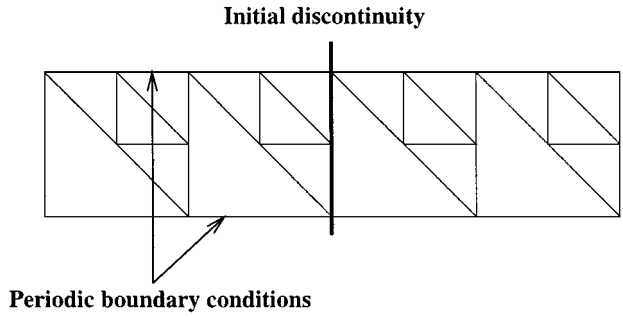

FIG. 5. Non-conformal triangulation for the shock tube problem. The full domain contains 4000 cells.

The 2D grid is shown in Fig. 5 and is a non-conformal triangulation. At time $t = 0$, the domain is separated in two parts. The initial data are

$$(\mathbf{u} = 0;\ \gamma = 2)$$

$$\rho_l = 1; \qquad B_{x,l} = 0.75; \qquad B_{y,l} = 1.; \qquad p_l = 1$$

$$\rho_r = 0.125; \qquad B_{x,r} = 0.75; \qquad B_{y,r} = -1.; \qquad p_r = 0.1.$$

The results are presented in Fig. 6 with $\tilde{\delta} = 0$. The variable B_n is plotted for $CFL = 1$; we can

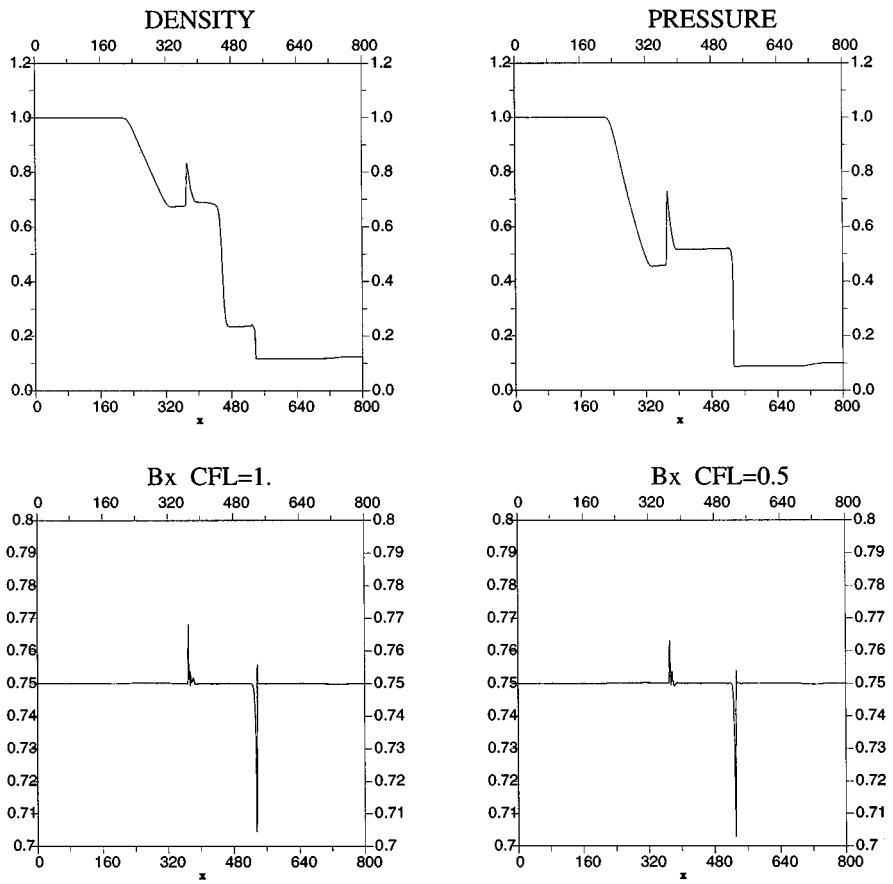

FIG. 6. Shock tube problem.

show an error of a few percent which does not decrease if we use a lower *CFL*. Nevertheless, no visible effects can be seen on the other variables.

The second test case concerns a reflected shock which has been proposed in [1]. The domain of the calculation is rectangular: $x \in [0, 3]$, $y \in [0, 1]$. This domain is larger than in [1] in order to see the area after the reflection. The boundary conditions are the following: The left and upper bondaries are fixed respectively with the values

$$(\gamma = 1.4)$$

$$\rho_l = 1; \qquad B_{x,l} = 0.5; \qquad B_{y,l} = B_{z,l} = 0.$$

$$u_l = 2.9; \qquad v_l = w_l = 0.; \qquad p_l = \frac{1}{\gamma}$$

$$\rho_r = 1.460; \qquad B_{x,r} = 0.68379; \qquad B_{y,r} = -0.1018; \qquad B_{z,r} = 0.$$

$$u_r = 2.716; \qquad v_r = -0.405; \qquad w_r = 0.; \qquad p_r = 1.223.$$

The lower boundary is reflective and the right boundary is an outgoing interface. The introduction of those boundary conditions is done in the following way.

We use "fictitious cells," which means that, for each boundary cell K (e denoting the edge on the boundary), we create a "fictitious cell" K_e out of the domain which is the mirror image of K about e. We set the values of variables in K_e regarding the type of boundary. For an outgoing interface, the values in K_e are the same as in K. For an inflow interface, the values in K_e correspond to the inflow variables. Finally, for a reflective boundary, the density, the pressure, and the tangential components of the magnetic field and the velocity in K_e are the same as in K and $\mathbf{B_{Ke}} \cdot \mathbf{n} = -\mathbf{B_K} \cdot \mathbf{n}$, $\mathbf{V_{Ke}} \cdot \mathbf{n} = -\mathbf{V_K} \cdot \mathbf{n}$ where $\mathbf{n}$ is the normal vector to the interface e.

At $t = 0$, the domain is initialized with the values of the left boundary. The solution of this problem is a steady state with a 29° shock.

The calculation has first been performed on an fine unstructured triangular grid (see Fig. 7) ($CFL = 0.8$ and $\tilde{\delta} = 0.2$). The result of B_x is presented in Fig. 8. We see that the shock and its reflection are well captured. Small variations are present in areas which are expected to be constant. However, it can be noted that the magnitude of those instabilities is less than 2% compared to the magnitude of the variable B_x. It's less than the order of the instabilities which have been observed for the shock tube test case. As it was expected [1], on rectangular meshes, the result is completely unstable (see Fig. 11).

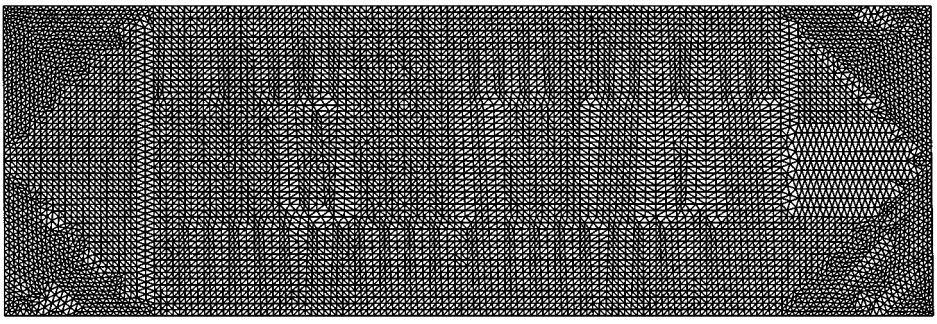

FIG. 7. Fine grid of 15,000 elements for the reflection problem.

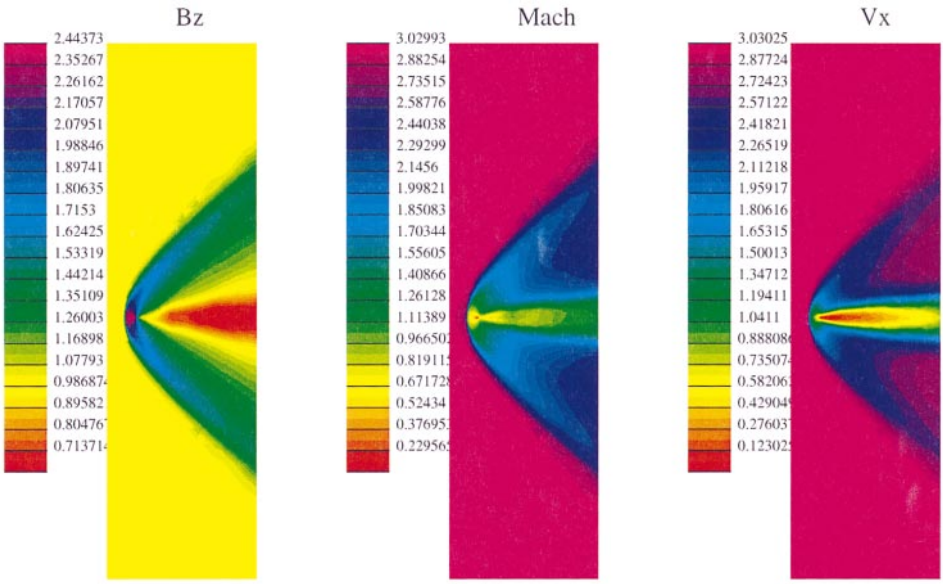

FIG. 20. Results of the mass loading simulation.

We have also performed the same test case on a initially coarse triangular grid after two refinement steps (see Fig. 9) in order to analyse the behaviour of the scheme on a non-conformal grid. The result is presented in Fig. 10 and compares quite well with those obtained on the conformal grid. The main difference is the presence of some numerical instabilities at the upper left corner, but their order of magnitude remains small. The convergence histories, on the refined grid and on the fine grid, are presented for the B_x variable during 15,000 time steps in Fig. 12. The residue at time t^n is defined as

$$\log\left(\int_x\int_y \left|B_x^n\right| dx\, dy - \int_x\int_y \left|B_x^{n-1}\right| dx\, dy\right). \tag{26}$$

The convergence level is higher on the refined grid because spurious oscillations in the uniform areas are lower on this grid than on the fine one. The B_x contours presented in [1] are more stable, but we emphasize the fact that our results have been obtained without any correction of **B** or modification of the MHD equations even on adaptively refined grids.

4. THE 2D SIMULATIONS ON ADAPTIVELY REFINED MESHES

4.1. *Interaction of a Plasma with a Cylinder*

The first 2D simulation concerns the interaction of a supersonic plasma with a perfectly conducting cylinder. Because of the 2D geometry, the only stable configuration is when the magnetic field is aligned with the cylinder axis (see [11]). Consequently, this problem corresponds to a hydrodynamic case with a special form of the state equation. The values of upstream physical data have been taken in the upstream conditions data for the interaction of the solar wind with planets (Mars, Venus, ...). After normalization [12] the upstream

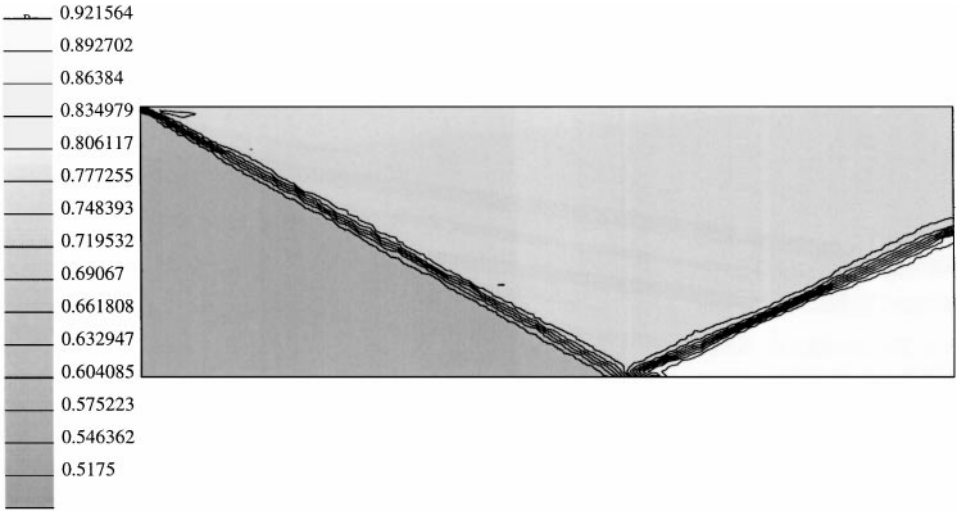

FIG. 8. *Bx* contours for the reflection problem on the fine grid.

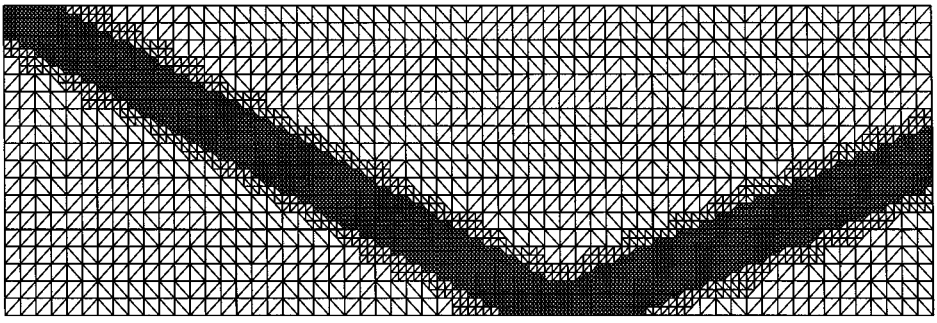

FIG. 9. Refined grid of 9000 elements for the reflection problem.

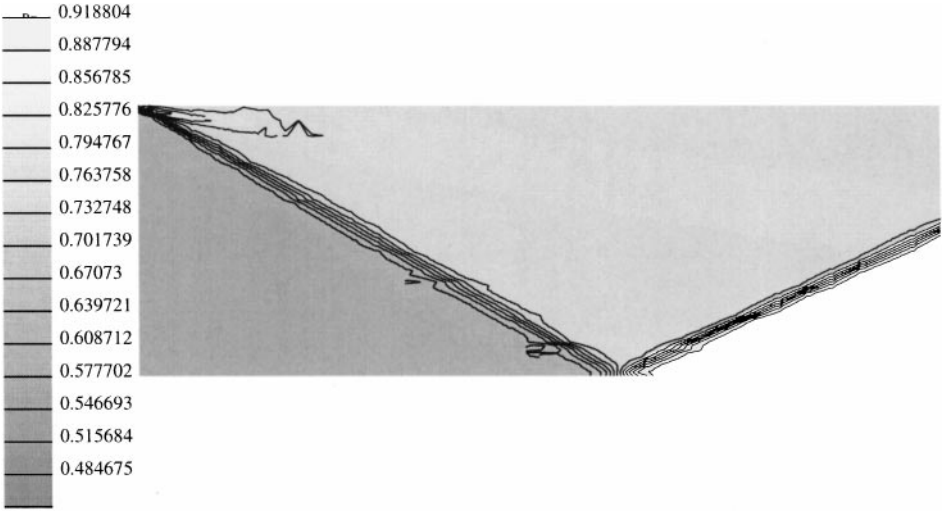

FIG. 10. *Bx* contours for the reflection problem on the refined grid.

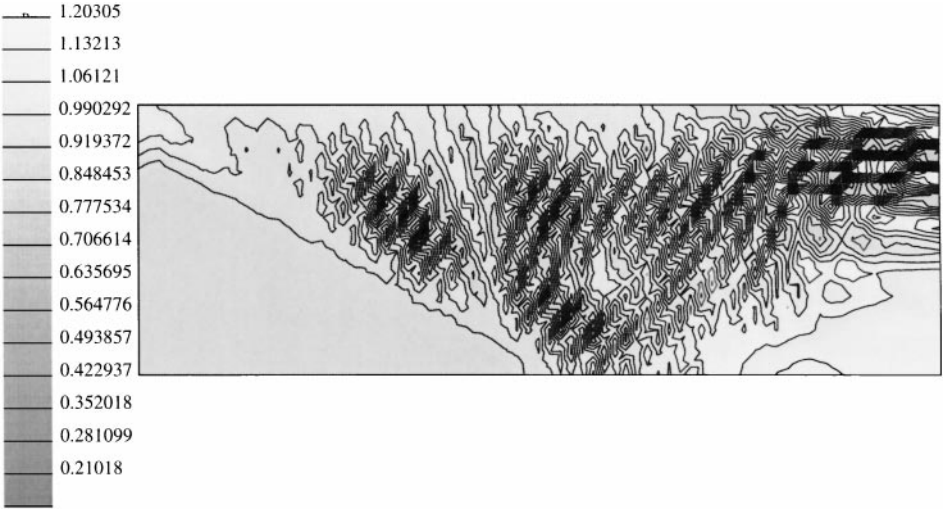

FIG. 11. *Bx* contours for the reflection problem on the cartesian grid.

dimensionless data values are ($\gamma = \frac{5}{3}$)

$$\begin{aligned} \tilde{\rho} &= 1 \\ \tilde{\mathbf{u}} &= \begin{pmatrix} 3 \\ 0 \\ 0 \end{pmatrix} \\ \tilde{p} &= 0.6 \\ \tilde{\mathbf{B}} &= \begin{pmatrix} 0 \\ 0 \\ 1 \end{pmatrix}. \end{aligned} \tag{27}$$

The unrefined full domain and the refined grid are shown in Fig. 13. The boundary conditions are the following: inflow for the left side and free stream conditions for the three others.

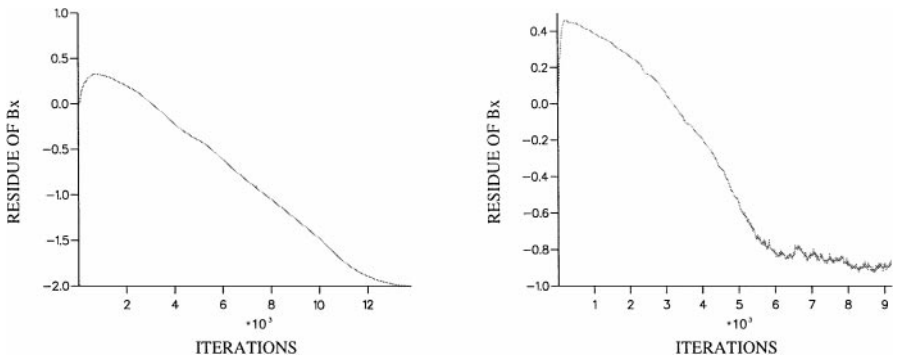

FIG. 12. Convergence histories for the reflection problem. The left figure concerns the refined grid for 15,000 time steps and the right one concerns the fine grid for 10,000 time steps.

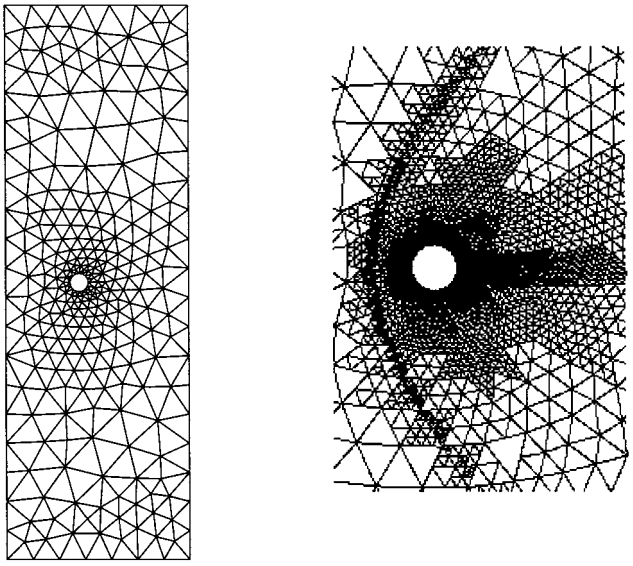

FIG. 13. The unrefined full domain and a part of the refined grid.

The refined grid has been obtained after 3 adaptation cycles. The initial coarse grid contained 500 cells and the final adapted one 7000. The convergence history for the density is presented in Fig. 14 for the three refinement steps. Numerical results are shown in Fig. 15: the perpendicular component of **B**, the mach number, and the component of the velocity

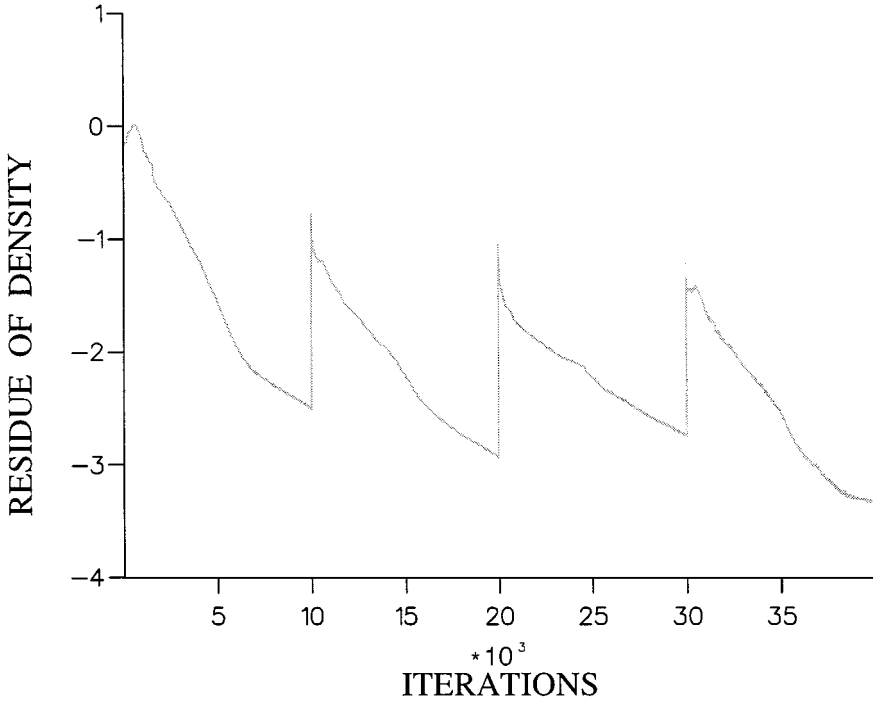

FIG. 14. Convergence on the density, for the three refinement steps.

parallel to the incoming flow have been plotted. For all the calculations we have chosen $\tilde{\delta} = 0.4$ and $CFL = 0.8$ in order to obtain a stable steady state.

As a comparison, we have performed the same calculation on two non-adapted grids: a medium one of 7000 elements and a reference fine one of 20,000 elements. The results are shown in Figs. 16 and 17. On the medium grid, the isovalues show a bad resolution of the shock and no recirculation behind the cylinder. On the other hand, the results on the fine and adapted grids are in very good agreement. The only significant difference is the small instability which can be seen between the shock and the cylinder on the fine grid. In case of the adapted mesh, the non-uniformity of the grid seems to prevent the apparition of such instabilities. We have performed the same test case on a very fine grid of 80,000 elements and the numerical results present the same features. A more precise comparison can be done, using the values of B_z along the $y = 0$ axis, represented on Fig. 18. The refined grid line and the cut line of the 80,000 elements grid are very similar. This proves the efficiency of the refinement procedure which gives accurate results in region of interest with an optimized number of cells.

4.2. *Mass Loading Simulation*

This second simulation is a 2D version of the cometary mass-loading problem. Around each comet, a neutral atmosphere is in expansion. The mass loading of the solar wind comes from the ionization of those neutral particules. It is this new cometary plasma that creates the interaction between solar wind and the comet. Because of the ionization scale ($\lambda = 10^6$ km) and the size of the cometary nucleus, we have to deal with different spatial scales. Unstructured triangular grids and automatic mesh refinement are very useful to perform this kind of calculation, because they permit a large range of cell size in the same mesh (even in the initial grid).

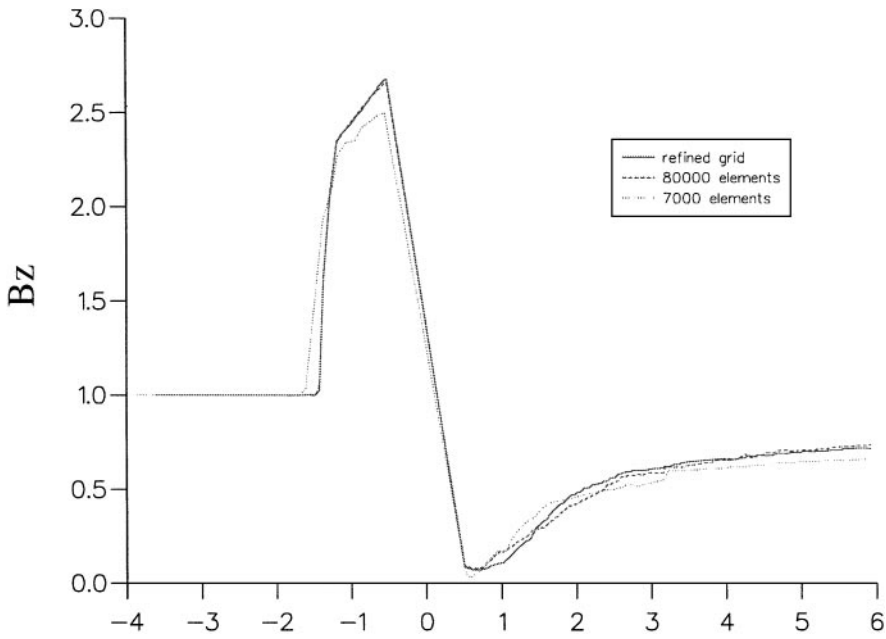

FIG. 18. Cut lines of B_z.

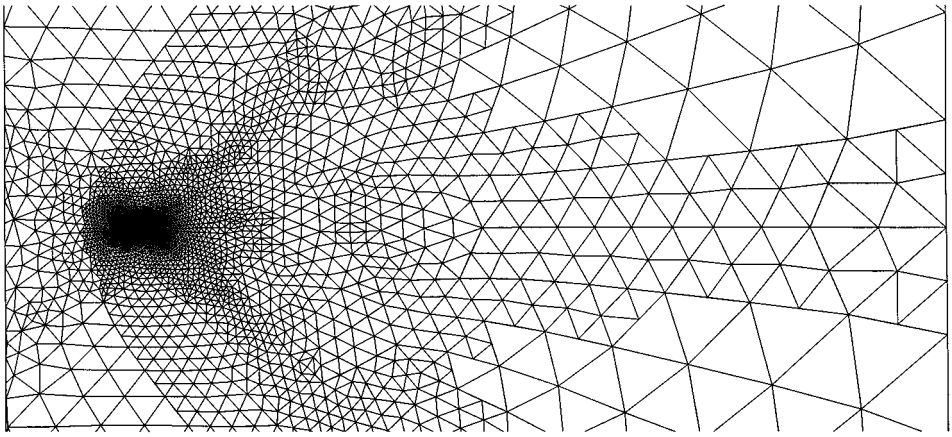

FIG. 19. Cometary interaction region of 13×28 ionization scale lengths.

The mass loading phenomena is introduced in the MHD equations with a source term for the continuity equation. Because of the small velocity ($\simeq 1$ km s^{-1}) and the weak energy of the new created cometary ions, the source terms on the other conservation equations are neglected in a first approximation. The mass source term is of the form

$$S = \tilde{S}\frac{e^{-\tilde{r}}}{\tilde{r}^2}, \tag{28}$$

where

$$\tilde{r} = \frac{r}{\lambda}$$

and $\tilde{S}$ is the dimensionless source coefficient. As in the first simulation, the 2D configuration

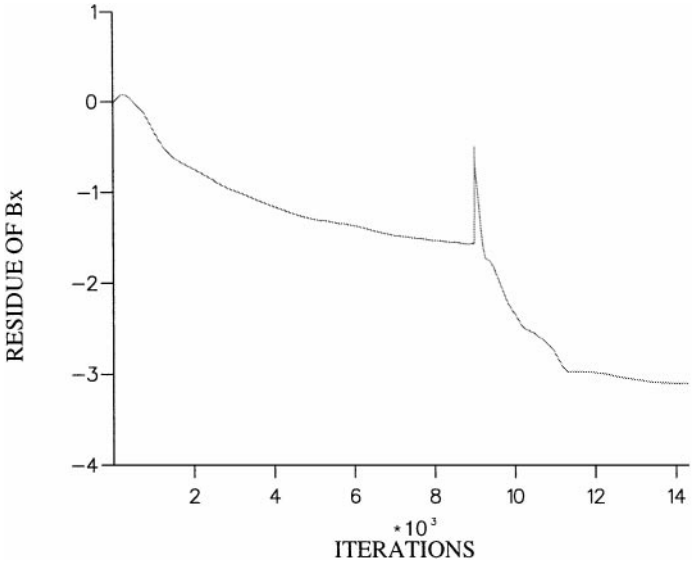

FIG. 21. Convergence history of B_z.

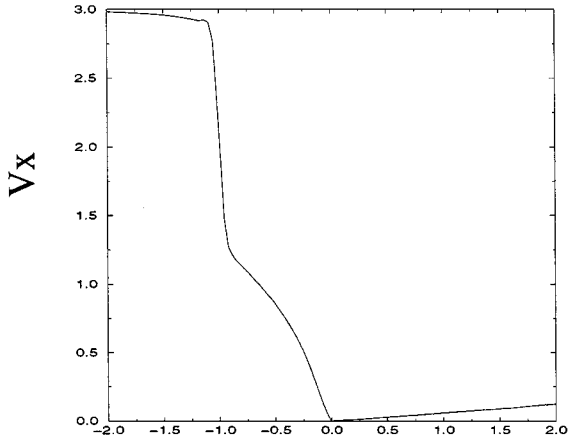

FIG. 22. Cut line of solar wind velocity along solar-comet line.

cannot reproduce the reality of the 3D interaction. Here we just want to prove that the code is able to treat multiscale problems. Figure 19 represents the grid in the region of the interaction. The entire simulation domain is of 24×72 ionization scale lengths. The radius of the central object is of $5 \cdot 10^{-5}$ ionization scale length. After the refinement procedure the number of cells in the adapted mesh is about 13,000.

Because of the very different scales of mesh size, a local time step technique has been used to accelerate the convergence to the steady state. Meanwhile, a upper limit has been introduced: the local time step was bounded by k times the smaller one and the value of k has been increased during the calculation (from 10 to 100).

The results are shown in Fig. 20. As in the case of the cylinder, we took $\tilde{\delta} = 0.4$ and $CFL = 0.8$ and the initial conditions of the inflow plasma are also the same. The calculation of the source parameter is done in [12] and it leads to $\tilde{S} = 5$. The resulting shock is located at one ionization scale length in front of the comet. The convergence history is plotted in Fig. 21 for the B_z variable. On the non-refined grid (9000 first time steps) we chose $k = 10$ for the upper limit of the local time step. On the refined grid (iterations 9000 to 15,000) this limit has been increased to 100. In Fig. 22 we have represented the solar wind velocity along the sun–comet line. Along this line the number of new created ions increases as the solar wind approaches the comet (situated at $x = 0.$), consequently the solar wind velocity decreases as we can see just before and behind the shock.

5. CONCLUSION

In this paper, we have presented a new numerical method for multidimensional MHD simulations. By adapting an idea of Bouchut [3], the weak consistency of our scheme with the constraint $\nabla \cdot \mathbf{B} = 0$ has been proved on triangular grids, even on non-conformal ones. The 2D numerical test cases have shown that this property seems to be sufficient to avoid numerical errors due to the non-exact preservation of this constraint. The 2D simulations of plasma flows have been performed and have shown the interest of using adaptively refined triangular grids to have a high order of precision, even for multiscale phenomena, with a low CPU and memory cost. Our main objective is now the application of this numerical method to 3D geometry with tetrahedral meshes.

ACKNOWLEDGMENT

The authors express their gratitude to Professor Degond for stimulating discussions and helpful comments.

REFERENCES

1. N. Aslan and T. Kammash, Developing numerical fluxes with new sonic fix for MHD equations, *J. Comput. Phys.* **133**, 43 (1997).
2. J. B. Bell, P. Colella, and J. A. Trangenstein, Higher order Godunov method for general systems of hyperbolic conservation laws, *J. Comput. Phys.* **82**, 362 (1989).
3. F. Bouchut, On the discrete conservation of the Gauss–Poisson equation of plasma physics, *Comm. Numer. Methods Eng.* **14**, 23 (1998).
4. M. Brio and C. C. Wu, An upwind differencing scheme for the equations of ideal magnetohydrodynamics, *J. Comput. Phys.* **75**, 400 (1988).
5. P. Cargo, *Nouveaux modèles numériques pour l'hydrodynamique atmosphérique et la magnétohydrodynamique idéale*, Ph.D. thesis, Université de Bordeaux I, France, 1995.
6. P. Cargo and G. Gallice, Roe matrices for ideal MHD and systematic construction of roe matrices for systems of conservation laws, *J. Comput. Phys.* **136**, 446 (1997).
7. J. P. Croisille, R. Khanfir, and G. Chanteur, Numerical simulation of the MHD equations by a kinetic-type method, *J. Sci. Comput.* **10**(1), 81 (1995).
8. W. Dai and P. Woodward, An approximate Riemann solver for ideal magnetohydrodynamics, *J. Comput. Phys.* **111**, 354 (1994).
9. W. Dai and P. Woodward, Extension of the piecewise parabolic method to multidimensional ideal magnetohydrodynamics, *J. Comput. Phys.* **115**, 485 (1994).
10. F. Dubois and G. Mehlman, A non parameterized entropy fix for Roe's method, *AIAA J.* **31**(1), 199 (1993).
11. G. Gallice, *Système d'Euler–Poisson, Magnétohydrodynamique et schéma de Roe*, Ph.D. Thesis, Université de Bordeaux I, France, 1997.
12. T. I. Gombosi, K. G. Powell, and D. L. De Zeeuw, Axisymmetric modeling of cometary mass loading on an adaptively refined grid: MHD results, *J. Geophys. Res.* **99**, 21,525 (1994).
13. A. Harten, High resolution schemes for hyperbolic conservations laws, *J. Comput. Phys.* **49**, 357 (1983).
14. K. G. Powell, *An Approximate Riemann Solver for Magnetohydrodynamics*, ICASE Report 94-24, 1994.
15. Progress and challenges in CFD methods and algorithms, in *Proc. 77th Fluid Dyn. Panel Symp., Agard Conf. Proc., 578, 1996.*
16. M. Schmidt-Voigt, Time-dependent MHD simulations for cometary plasmas, *Astron. Astrophys.* **210**, 433 (1989).
17. T. Tanaka, Configurations of the solar wind flow and magnetic field around the planets with no magnetic field: Calculation by a new MHD simulation scheme, *J. Geophys. Res.* **98**, 17,251 (1993).
18. P. Villedieu, *Analyse numérique appliquée à la mécanique des fluides*, Technical Report 2/3526.00/DERIGAN, ONERA, France, 1995.
19. L. C. Woods, *Principles of Magnetoplasma Dynamics* (Clarendon, Oxford, 1987).
20. H. C. Yee, G. H. Klopper, and J. L. Montagné, High-resolution shock-capturing schemes for inviscid and viscous hypersonic flows, *J. Comput. Phys.* **88**, 31 (1990).
21. A. L. Zachary and P. Colella, A higher-order Godunov method for the equations of ideal magnetohydrodynamics, *J. Comput. Phys.* **99**, 341 (1992).